OCTOBER 16 2025

On the sound pressure distribution in the inner ear induced by rigid body vibration

Simon Kersten ; Henning Taschke; Michael Vorländer

J. Acoust. Soc. Am. 158, 3006–3016 (2025)
https://doi.org/10.1121/10.0039575

JASA ARTICLE

On the sound pressure distribution in the inner ear induced by rigid body vibration

Simon Kersten,[1,a] Henning Taschke,[2] and Michael Vorländer[1]
[1]*Institute for Hearing Technology and Acoustics, RWTH Aachen University, 52074 Aachen, Germany*
[2]*44869 Bochum, Germany*

ABSTRACT:
Intracochlear sound pressure measurements are essential for understanding inner ear function. During bone conduction (BC) stimulation, these pressures exhibit pronounced variability and similar magnitudes in the two scalae, making their interpretation challenging. These characteristics arise from the vibration of the entire inner ear and interactions between the different BC mechanisms. Using fundamental acoustic principles, we derive characteristics of intracochlear pressure distributions driven by fluid inertial effects from rigid body vibration of the inner ear. Our analysis shows that the vibration at a spatially uniform velocity in a single direction results in (1) proportionality of the pressure to stimulation velocity and frequency, (2) a linear pressure variation along the vibration direction, (3) uniform pressure in planes perpendicular to the motion, and (4) minimum pressure at a plane approximately aligned with the round window centroid. The superposition principle allows the extension of these results to any complex-valued amplitude vector of rigid body translation. The findings provide insights into the variability of experimental intracochlear sound pressure measurements and enhance the understanding of the interactions between the mechanisms involved in BC hearing.
 https://doi.org/10.1121/10.0039575
(Received 5 March 2025; revised 20 August 2025; accepted 28 September 2025; published online 16 October 2025)
[Editor: Hideko Heidi Nakajima] Pages: 3006–3016

I. INTRODUCTION

Intracochlear sound pressure measurements are a well-established method for studying the inner ear's response to sound stimulation. During air-conducted (AC) stimulation, scala vestibuli and scala tympani pressures differ significantly in both magnitude and frequency response, enabling distinct determination of differential sound pressure (Nakajima *et al.*, 2009; Frear *et al.*, 2018), which is a key indicator for auditory perception (Dancer and Franke, 1980). In this case, the sound follows a relatively straightforward path from the ear canal through the middle ear, and enters the inner ear via the oval window (OW), ultimately generating a traveling wave in the basilar membrane (BM) and causing deflection of the round window (RW) membrane.

In contrast, during bone conduction (BC) stimulation, measured scala vestibuli and scala tympani pressures exhibit similar magnitudes and frequency responses (Stieger *et al.*, 2018; Mattingly *et al.*, 2020; Geerardyn *et al.*, 2024). When normalized to promontory velocity, these pressures show pronounced peaks and notches, and substantial inter-individual variability, with 95% confidence intervals spanning up to 40 dB (Stieger *et al.*, 2018; Dobrev *et al.*, 2022; Dobrev *et al.*, 2023). These characteristics pose challenges for interpreting the experimental data.

These effects can be partially attributed to the inner ear's three-dimensional, frequency-dependent motion during BC stimulation. Cadaver head measurements and numerical simulations with excitation by BC hearing aids suggest predominantly rigid body vibration of the otic capsule up to approximately 7–10 kHz, with the direction of motion varying with frequency (Dobrev *et al.*, 2023; Dobrev *et al.*, 2025). This finding aligns with the notion that, in this frequency range, structural wavelengths in the surrounding bone and fluid wavelengths are significantly larger than the inner ear's dimensions. For instance, with a speed of sound of 400 m/s in the surrounding bone (Stenfelt, 2015) and 1500 m/s in the cochlear fluid (comparable to water), the wavelengths at 1 kHz are 0.4 and 1.5 m, respectively. These values exceed the dimensions of the inner ear (Purcell *et al.*, 2003) by at least an order of magnitude. This supports the approximation of rigid body vibration of the inner ear at lower frequencies. Such rigid body vibration is closely linked to cochlear fluid inertia effects (Stenfelt, 2015), identified as the primary mechanism for the inner ear's response during BC stimulation in lumped element simulations combined with measured transfer functions (Stenfelt, 2016, 2020). Finite element simulations further highlighted the directionality of this BC mechanism (Kim *et al.*, 2014).

Another contributor to the variability in intracochlear pressure measurements is the interaction of fluid inertia with other BC mechanisms, including inertia of the ossicles, inner ear compression, and pressure transmission from the

[a]Email: simon.kersten@akustik.rwth-aachen.de

https://doi.org/10.1121/10.0039575

skull interior (Tonndorf, 1968; Stenfelt and Goode, 2005a). The frequency-dependent contributions of these mechanisms and the detailed interaction between the inner ear's motion and the fluid dynamics during measurements remain poorly understood, complicating the normalization of intracochlear pressures to reference quantities, such as ear canal sound pressure, stapes velocity, or adjacent bone velocity (Stieger *et al.*, 2018).

The central question in this context is how sound pressure behaves within a fluid enclosed in a cavity subjected to rigid body vibration. By analytically solving the sound field in a tube with same-phase disturbances at its ends, Rayleigh (1945) was the first to demonstrate that such forced vibration can cause the sound pressure in fluids to be zero in magnitude at certain positions, even at frequencies below the occurrence of resonance effects. While this phenomenon could contribute to the variability observed in intracochlear pressure measurements, its significance in the context of BC stimulation of the inner ear has, to our knowledge, yet to be explored.

In this study, we aim to provide a theoretical foundation for understanding the intracochlear sound pressure distributions during BC stimulation. We derive the characteristics of these distributions based on fundamental fluid dynamics principles, focusing on the effects of rigid body vibration of the inner ear due to a uniform vibration velocity of the inner ear's surroundings. This analysis offers explanations for the characteristics of intracochlear sound pressure measurements and enhances our understanding of the mechanisms underlying BC hearing.

II. METHODS

A. Definitions and simplifications

1. Vibration velocity

To derive an analytical expression for the low-frequency sound pressure distribution in the inner ear during BC stimulation, we assume that the structures surrounding the inner ear vibrate uniformly at a velocity $\mathbf{v}_0\, e^{j\omega t}$. Here, $\mathbf{v}_0$ represents the amplitude vector with three complex-valued Cartesian components, j is the imaginary unit, ω is the angular frequency, and t denotes time. For brevity, we omit the explicit oscillatory term $e^{j\omega t}$ in all subsequent expressions.

In the skull base of cadaver heads, where the inner ear is embedded within a complex structure composed of cortical bone, diploë, and various soft tissues, measured wave speeds are approximately 400 m/s (Stenfelt and Goode, 2005b). Based on this, and assuming a threshold of one-tenth of the wavelength relative to inner ear dimensions of 10–15 mm, the conservative upper frequency limit for considering the inner ear vibration to be dominated by rigid body motion is estimated to lie above 2–3 kHz.

Note that the assumption of a uniform velocity considers only the rigid body translation of the inner ear, neglecting the effects of rigid body rotation. However, as discussed in Sec. IV, the translational case already provides fundamental insights into the intracochlear sound pressure distributions associated with rotational rigid body vibration of the inner ear during BC.

We decompose the resulting vibration of the cochlear fluid into a common motion component, $\mathbf{v}_0$, which equals the vibration of the surrounding structures, and a differential motion component, $\mathbf{v}_{\text{diff}}$, which captures velocity deviations from $\mathbf{v}_0$,

$$\mathbf{v}(\mathbf{x}) = \mathbf{v}_0 + \mathbf{v}_{\text{diff}}(\mathbf{x}). \tag{1}$$

Here, $\mathbf{v}(\mathbf{x})$ and $\mathbf{v}_{\text{diff}}(\mathbf{x})$ represent the particle velocity and the differential velocity in the fluid at a spatial position $\mathbf{x}$, each consisting of three complex-valued Cartesian components. Notably, $\mathbf{v}_0$ is independent of the position. Equation (1) extends the approach of Stenfelt (2015), where a similar decomposition into common and differential motion was applied to the vibration of the cochlear boundaries.

When the fluid wavelength is significantly larger than the dimensions of the inner ear, the condition $||\mathbf{v}_0|| \gg ||\mathbf{v}_{\text{diff}}(\mathbf{x})||$ holds, where $||\cdots||$ denotes the Euclidean norm computed from the magnitudes of the Cartesian components. Under this condition, Eq. (1) simplifies to

$$\mathbf{v}(\mathbf{x}) \approx \mathbf{v}_0. \tag{2}$$

This approximation indicates that the fluid primarily follows the rigid body vibration of its surrounding structures. It is important to note that this approximation does not imply $\mathbf{v}_{\text{diff}}$ to be zero, as non-zero differential motion across the cochlear partition is essential for driving the BM traveling wave.

2. Impedance boundaries

The non-rigid boundaries and outlets of the inner ear, such as the RW, OW, surfaces of the osseous spiral lamina, or vestibular and cochlear aqueducts, are incorporated through their respective surface areas, S_k, and acoustic impedances, Z_k, or admittances, Y_k (see also Stenfelt, 2016, 2020; Guan *et al.*, 2020; Kersten *et al.*, 2025), with an arbitrary index k. Such incorporation is valid here since we only consider wavelengths in the fluid which are significantly larger than the dimensions of these boundaries.

This approach excludes any sound entering the inner ear that is not related to the rigid body vibration. This distinction is especially important for the OW. For AC stimulation, stapes vibration depends on the input impedance of the inner ear and serves as the source of intracochlear pressure. Likewise, BC pathways via the OW involve relative motion between the stapes footplate and surrounding bone due to forward-propagating sound. In contrast, we here incorporate the OW solely through a "reverse middle ear impedance" (Puria, 2003; Frear *et al.*, 2018), meaning the stapes footplate responds with relative motion as a consequence of sound pressure acting on it from within. Nevertheless, the principle of superposition allows the effects of additional

contributors, particularly the AC and BC contributions entering via the OW, to be considered separately from the rigid body vibration (see Sec. IV).

The centroids of the impedance surfaces are defined as

$$\bar{\mathbf{x}}_k = \frac{1}{S_k}\int_{S_k} \mathbf{x}\,\mathrm{d}S. \tag{3}$$

Following Pierce (2019), the impedances Z_k and admittances Y_k are given by

$$Z_k = \frac{\bar{p}_k}{q_{k,\mathrm{diff}}} = \frac{1}{Y_k}, \tag{4}$$

where $\bar{p}_k$ denotes the surface-averaged pressure,

$$\bar{p}_k = \frac{1}{S_k}\int_{S_k} p(\mathbf{x})\,\mathrm{d}S, \tag{5}$$

and $q_{k,\mathrm{diff}}$ represents the differential volume velocity,

$$q_{k,\mathrm{diff}} = Y_k\,\bar{p}_k = \frac{Y_k}{S_k}\int_{S_k} p(\mathbf{x})\,\mathrm{d}S = \int_{S_k} \mathbf{v}_{\mathrm{diff}}(\mathbf{x})\cdot\mathbf{n}(\mathbf{x})\,\mathrm{d}S. \tag{6}$$

Here, $\mathbf{n}(\mathbf{x})$ denotes the outward normal vector on the surface. The quantities used in Eqs. (3)–(6) are illustrated in Fig. 1 (left). As shown, the surfaces S_k need not be flat for these equations to hold.

It is important to note that $q_{k,\mathrm{diff}}$ is often not distinguished from the volume velocity determined solely from $\mathbf{v}(\mathbf{x})$ without considering the differential velocity $\mathbf{v}_{\mathrm{diff}} = \mathbf{v}(\mathbf{x}) - \mathbf{v}_0$ in Eq. (6). This simplification is valid when the fluid cavity of interest remains stationary ($\mathbf{v}_0 = 0$). However, if the cavity enclosing the fluid undergoes vibration, its motion must be explicitly accounted for in the impedance/admittance boundary condition (Suzuki *et al.*, 1989; Marburg and Anderssohn, 2011). To illustrate, consider a rigid surface with $Z_k \to \infty$ and $Y_k \to 0$. In this case, the infinite impedance results in a differential volume velocity $q_{k,\mathrm{diff}}$ of zero, while the vibration at velocity $\mathbf{v}_0$ still leads to a nonzero total volume velocity associated with the surface.

Furthermore, we account for the compliance of the fluid volume V in terms of its impedance, Z_c, and an admittance, Y_c, as (see Sec. 7.2.5. in Pierce, 2019)

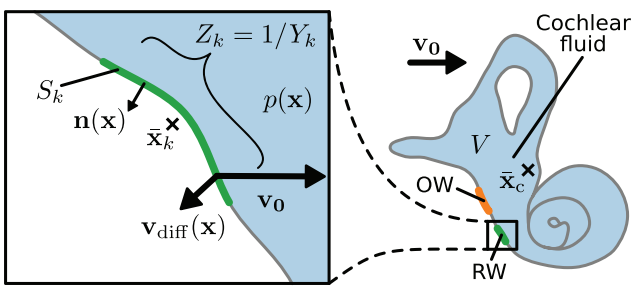

FIG. 1. Schematic illustration of the quantities used in Eqs. (3)–(8). The RW is shown as a representative example for the surface-based quantities.

$$Z_c = \frac{\rho c^2}{j\omega V} = \frac{1}{Y_c}, \tag{7}$$

where ρ is the fluid density and c is the speed of sound. The centroid of the fluid volume, illustrated in Fig. 1 (right), is defined as

$$\bar{\mathbf{x}}_c = \frac{1}{V}\int_V \mathbf{x}\,\mathrm{d}V. \tag{8}$$

B. Derivation of the sound pressure distribution

We begin the derivation of the sound pressure distribution by employing Euler's equation [Pierce, 2019, their Eq. (1.3.6)] which, for an oscillation $e^{j\omega t}$, reads

$$\nabla p(\mathbf{x}) = -\rho[j\omega\,\mathbf{v}(\mathbf{x}) + [\mathbf{v}(\mathbf{x})\cdot\nabla]\mathbf{v}(\mathbf{x})], \tag{9}$$

where $\nabla p(\mathbf{x})$ denotes the gradient of the pressure phasor $p(\mathbf{x})$ at position $\mathbf{x}$. The term $[\mathbf{v}(\mathbf{x})\cdot\nabla]\mathbf{v}(\mathbf{x})$ presents the convective derivative of the velocity field. This term vanishes when applying the approximation $\mathbf{v}(\mathbf{x}) \approx \mathbf{v}_0$ from Eq. (2). Thereby, Eq. (10) is simplified to Newton's law, which states that the pressure gradient is proportional to the acceleration of the fluid:

$$\nabla p(\mathbf{x}) = -j\omega\rho\,\mathbf{v}_0. \tag{10}$$

A natural solution to Eq. (10) is the linear function

$$p(\mathbf{x}) = -j\omega\rho\mathbf{v}_0\cdot(\mathbf{x} - \mathbf{x}_0), \tag{11}$$

where $\mathbf{x}_0$ denotes a yet unknown (complex-valued) position vector.

The condition that the differential velocity is small compared to the total particle velocity [Eq. (2)] results in the slope of the pressure function of $-j\omega\rho\mathbf{v}_0$. However, to determine $\mathbf{x}_0$, the differential velocity may not be neglected. Instead, we need to account for the fact that any change in pressure within the fluid is balanced by the net outward volume velocity (see Sec. 7.3.2. in Pierce, 2019),

$$\begin{aligned} -j\omega\int_V \frac{p(\mathbf{x})}{\rho c^2}\,\mathrm{d}V &= \oint_{\partial V} \mathbf{v}(\mathbf{x})\cdot\mathbf{n}(\mathbf{x})\,\mathrm{d}S \\ &= \oint_{\partial V} [\mathbf{v}_0 + \mathbf{v}_{\mathrm{diff}}(\mathbf{x})]\cdot\mathbf{n}(\mathbf{x})\,\mathrm{d}S \\ &= \oint_{\partial V} \mathbf{v}_0\cdot\mathbf{n}(\mathbf{x})\,\mathrm{d}S + \sum_k q_{k,\mathrm{diff}} \\ &= \sum_k q_{k,\mathrm{diff}}, \end{aligned} \tag{12}$$

where $\oint_{\partial V}\cdots\mathrm{d}S$ denotes an integration over the entire surface of the fluid volume V. Here, Stokes' theorem is applied, showing that the net volume velocity contribution associated with $\mathbf{v}_0$ is zero. Therefore, only the differential volume velocities $q_{k,\mathrm{diff}}$ corresponding to the outlets and non-rigid surfaces remain.

https://doi.org/10.1121/10.0039575

Note that these surfaces include the cochlear partition. For example, a differential volume velocity may be attributed to vibration of the osseous spiral lamina, even though it primarily follows the overall stimulation velocity (Kersten *et al.*, 2025), and thus satisfies Eq. (2). In contrast, vibration associated with the BM traveling wave does not contribute to a net volume velocity, as the outward differential motion in one scala is exactly canceled by inward differential motion in the other when evaluated over the surface integral in Eq. (12). Although separating the integrals in Eq. (12) into contributions from the scala vestibuli and scala tympani is theoretically possible, doing so would unnecessarily complicate the derivation without offering further insight.

Inserting the pressure function [Eq. (6)] and differential volume velocity definition [Eq. (11)] yields

$$-\frac{j\omega}{\rho c^2}\int_V -j\omega\rho\mathbf{v}_0\cdot(\mathbf{x}-\mathbf{x}_0)\,\mathrm{d}V = \sum_k \frac{Y_k}{S_k}\int_{S_k} -j\omega\rho\mathbf{v}_0\cdot(\mathbf{x}-\mathbf{x}_0)\,\mathrm{d}S. \tag{13}$$

Since $-j\omega\rho\mathbf{v}_0 \neq \mathbf{0}$ per definition, Eq. (13) can be rewritten as

$$\left[Y_\mathrm{c}+\sum_k Y_k\right]\mathbf{x}_0 = Y_\mathrm{c}\bar{\mathbf{x}}_\mathrm{c}+\sum_k Y_k\bar{\mathbf{x}}_k,$$
$$\mathbf{x}_0 = \frac{Y_\mathrm{c}\bar{\mathbf{x}}_\mathrm{c}+\sum_k Y_k\bar{\mathbf{x}}_k}{Y_\mathrm{c}+\sum_k Y_k}. \tag{14}$$

Equation (14) identifies $\mathbf{x}_0$ as the admittance-weighted average of the centroids of the fluid volume and its non-rigid boundaries. Since the admittance terms are frequency-dependent, $\mathbf{x}_0$ may shift with frequency. Furthermore, the complex-valued nature of the surface admittances results in a complex-valued $\mathbf{x}_0 = \Re\{\mathbf{x}_0\}+j\Im\{\mathbf{x}_0\}$. Since $\mathbf{x}$ is real-valued, the resulting pressure distribution can be expressed as

$$\Re\{p(\mathbf{x})\} = -\omega\rho\mathbf{v}_0\cdot\Im\{\mathbf{x}_0\},$$
$$\Im\{p(\mathbf{x})\} = -\omega\rho\mathbf{v}_0\cdot\big(\mathbf{x}-\Re\{\mathbf{x}_0\}\big), \tag{15}$$

which shows that the real part of the pressure is spatially constant, while the imaginary part decreases linearly with $\mathbf{x}$. These characteristics are discussed in detail in Sec. III. The negative sign in the real part of Eq. (15) reflects the phase relationship to $\mathbf{v}_0$ and to the imaginary part of $\mathbf{x}_0$, whose sign depends on the specific values of the boundary admittances [Eq. (14)]. These admittances can exhibit either positive or negative imaginary components, corresponding to compliance-like or inertial behavior, respectively.

Equation (14) includes the case where the fluid is entirely enclosed by rigid boundaries. In this scenario, $\mathbf{x}_0$ simply coincides with the centroid of the fluid volume, $\bar{\mathbf{x}}_\mathrm{c}$. However, when the surrounding boundaries include surfaces with nonzero admittances, $\mathbf{x}_0$ shifts accordingly. At the inner ear, the RW membrane can be considered the most compliant surface. Therefore, it is reasonable to approximate $\mathbf{x}_0$ as

$$\mathbf{x}_0 \approx \bar{\mathbf{x}}_\mathrm{rw} = \frac{1}{S_\mathrm{rw}}\int_{S_\mathrm{rw}} \mathbf{x}\,\mathrm{d}S. \tag{16}$$

It is noteworthy that Eq. (16) refers solely to the membrane surface itself, corresponding to the compliance component in measured acoustic impedances of the RW. These impedances reflect not only the membrane's compliance but also the influence of adjacent fluid in the scala tympani (Frear *et al.*, 2018; Kersten *et al.*, 2024). As frequency increases, the contribution of the membrane's compliance to the measured impedance diminishes, while the fluid's contribution causes a magnitude increase above approximately 0.5–1 kHz (Frear *et al.*, 2018).

C. Vibration along a single direction

For clearer illustration in the following, we consider the vibration to occur exclusively along a single direction, denoted as x, with a velocity magnitude of v_0, as shown in Fig. 2. Thereby, Eqs. (11) and (15) simplify to

$$p(x) = -j\omega\rho v_0(x-x_0),$$
$$\Re\{p(x)\} = -\omega\rho v_0\Im\{x_0\},$$
$$\Im\{p(x)\} = -\omega\rho v_0(x-\Re\{x_0\}), \tag{17}$$

with $x_0 \approx \bar{x}_\mathrm{rw}$ denoting the x component of $\mathbf{x}_0$. It is important to emphasize that restricting the analysis to vibration in a single direction does not limit the generality of the results. Any complex-valued amplitude vector of rigid body vibration can be decomposed into three orthogonal components, each representing a one-dimensional translation with a specific phase. As a result, the overall pressure distribution can be determined by superimposing the individual distributions corresponding to each velocity component.

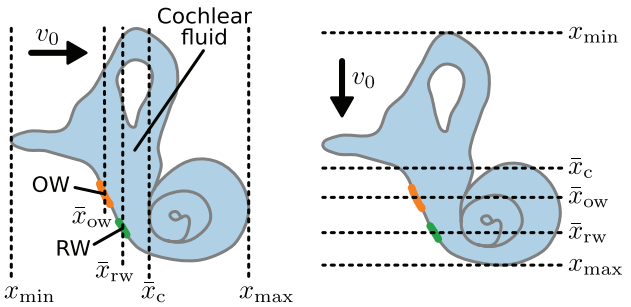

FIG. 2. Schematic illustration of the inner ear undergoing rigid body vibration at velocity v_0 in two example directions. Dotted lines indicate planes perpendicular to the motion direction at the spatial limits of the inner ear along the direction of motion (x_min and x_max), as well as at the centroids of the fluid volume ($\bar{x}_\mathrm{c}$), OW ($\bar{x}_\mathrm{ow}$), and RW membrane ($\bar{x}_\mathrm{rw}$).

D. Example calculations

For the following example sound pressure distributions, we included three surface admittances based on values inferred from cochlear impedance measurements reported by Frear *et al.* (2018) to calculate x_0 according to Eq. (14). Specifically, we modeled the RW as a compliance of 3.59×10^{14} m^3/Pa, obtained by isolating the compliance term from the RW impedance model of Frear *et al.* (2018) to remove the contribution of adjacent fluid. The OW was modeled as a series resonator with parameters $R = 4.76 \times 10^{10}$ Pas/m^3, $L = 7.78 \times 10^5$ Pas^2/m^3, and $C = 2.56 \times 10^{-15}$ m^3/Pa (Frear *et al.*, 2018). Vestibule and scala vestibuli leakage was modeled as a resistance $R = 9.8 \times 10^{10}$ Pas/m^3 in series with an inductance $L = 5 \times 10^6$ Pas^2/m^3 (Frear *et al.*, 2018). Assuming an inner ear volume of $V \approx 190$ mm^3 (Hiller *et al.*, 2020), a fluid density of 1000 kg/m^3, and a sound speed of 1500 m/s, we calculated the compliance of the inner ear fluid [given by $V/(\rho c^2)$, see Eq. (7)] as 8.44×10^{-17} m^3/Pa. Additionally, we assumed a representative inner ear dimension of $x_{max} - x_{min} = 8.4$ mm (Stenfelt, 2015). Approximately matching the left panel of Fig. 2, we positioned the fluid centroid $\bar{x}_c$ at 55% of the distance between x_{min} and x_{max}, aligned the vestibuli leakage with $\bar{x}_c$, and set the RW and OW centroids to $\bar{x}_{rw} = \bar{x}_c - 1$ mm and $\bar{x}_{ow} = \bar{x}_c - 2$ mm. The Python code used for these calculations is provided in the supplementary material.

III. RESULTS

A. Key features of the sound pressure distribution

Equation (17) indicates key characteristics of the intracochlear sound pressure distribution resulting from rigid body vibration of the inner ear along a single direction:

- The sound pressure is proportional to both frequency and the translation velocity. These characteristics reflect the inertial behavior of the fluid.
- The sound pressure is constant in planes perpendicular to the vibration direction. This follows from the unidirectional nature of the vibration, which results in an absence of pressure gradients in the orthogonal directions.
- Referenced to the vibration velocity, the imaginary part of the sound pressure linearly decreases along the vibration direction, while the real part is constant.
- The sound pressure exhibits a plane of minimum magnitude. This feature arises from mass conservation. In an enclosed system with rigid boundaries, this plane aligns with the centroid of the fluid volume. In the inner ear, the compliance of the RW membrane shifts this plane toward the centroid of the RW membrane.

B. Illustration of the sound pressure distribution

To further illustrate these characteristics, we now present multiple visualizations of the sound pressure distribution.

Figure 3 shows the magnitude, phase, real, and imaginary components of the sound pressure at an example frequency of 1 kHz, referenced to the phase of the vibration velocity. The spatial limits of the inner ear in the vibration direction are denoted as x_{min} and x_{max}, with example centroids of the fluid, $\bar{x}_c$, of the OW, $\bar{x}_{ow}$, and of the RW membrane, $\bar{x}_{rw}$, as illustrated in the left panel of Fig. 2.

Following Eq. (17), the imaginary part in Fig. 3 decreases linearly from a maximum (22.4×10^3 Pa s/m) to a minimum value (-30.4×10^3 Pa s/m) with a sign change at $x \approx \bar{x}_{rw}$. The real part of the pressure remains constant across all positions (44.1 Pa s/m). It is small compared to the imaginary part, except at the zero-crossing of the imaginary part. Consequently, the pressure magnitude exhibits linear spatial relationships for $x < \bar{x}_{rw}$ and $x > \bar{x}_{rw}$, with magnitudes reaching maximum values at x_{min} and x_{max}. At $x \approx \bar{x}_{rw}$, the magnitude reaches a minimum equal to the real part, and the phase transitions from $+\pi/2$ to $-\pi/2$. With all boundaries rigid, the minimum would coincide with the fluid centroid at $\bar{x}_c$. However, the compliance of the RW membrane shifts the minimum close to the RW centroid.

Figure 4 illustrates the magnitude of the sound pressure distribution on a logarithmic scale, depicted for a color-coded frequency range from 100 Hz to 4 kHz. The upper frequency limit reflects the approximate applicability of the low-frequency assumptions on the rigid body vibration, corresponding to one-tenth of the fluid wavelength in the

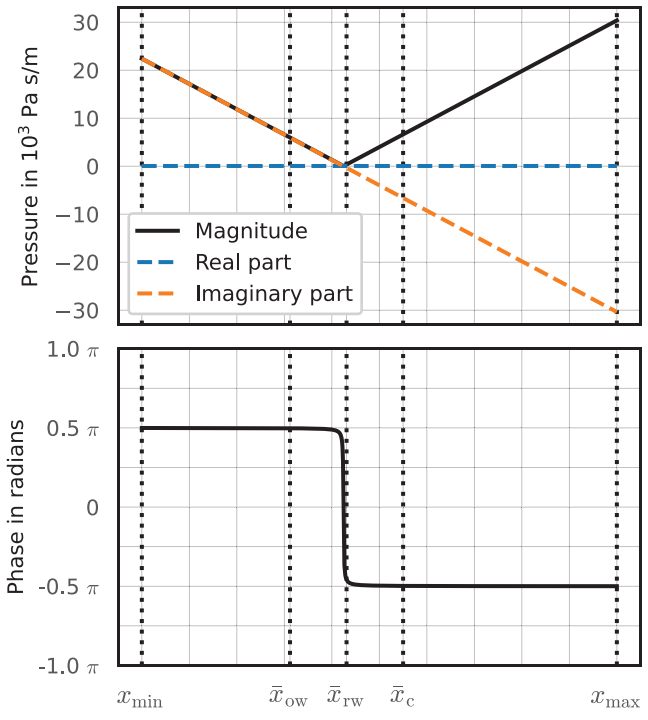

FIG. 3. Sound pressure distribution in the inner ear during rigid body vibration in terms of magnitude and phase, as well as real and imaginary parts. Dotted vertical lines indicate the spatial limits of the inner ear in the direction of motion (x_{min} and x_{max}), and centroids of the fluid volume ($\bar{x}_c$), OW ($\bar{x}_{ow}$), and RW membrane ($\bar{x}_{rw}$). This example pressure is normalized to the vibration velocity and calculated at a frequency of 1 kHz, based on parameters detailed in Sec. II D.

https://doi.org/10.1121/10.0039575

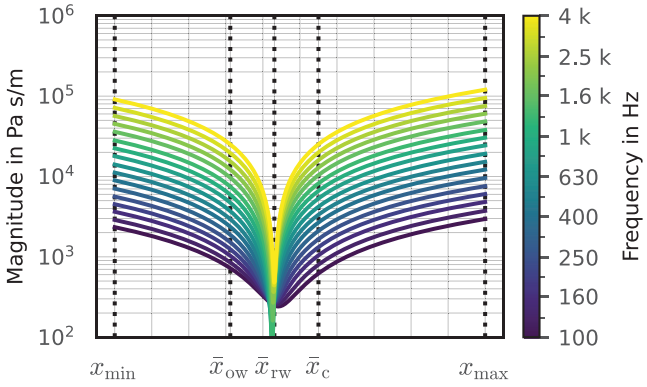

FIG. 4. Sound pressure distribution on a logarithmic scale for a color-coded frequency range from 100 Hz to 4 kHz, matching the schematic illustration in the left panel of Fig. 2 and calculated based on parameters detailed in Sec. II D.

uncoiled human cochlea (3.5 cm), and on the cochlear impedances. The pressure magnitudes, normalized to the vibration velocity v_0, correspond well to measured intracochlear sound pressures in the scala vestibuli, normalized to the velocity of the cochlear bone, which typically range from 3×10^3–3×10^5 Pa s/m (Stieger *et al.*, 2018; Dobrev *et al.*, 2022; Geerardyn *et al.*, 2024).

The logarithmic representation in Fig. 4 transforms the linear relationship between pressure and position from Eqs. (11) and (17), as depicted in Fig. 3, into a distribution characterized by a notch which shifts slightly around $\bar{x}_{\mathrm{rw}}$ with frequency due to frequency dependence of the surface admittances. At locations away from this minimum, the pressure magnitudes scale proportionally with frequency, corresponding to an increase with 20 dB per decade. With a zero real part of the pressure distribution, the magnitude would theoretically approach minus infinity decibels at this point. However, the finite real part at this location leads to a minimum value instead, which varies in magnitude with frequency due to its proportionality to ω [Eq. (17)] and the frequency-dependent surface admittances influencing x_0 [Eq. (14)]. As a result, the range of magnitudes in the sound pressure distribution depends on the frequency as well, highlighting the combined dependence of the sound pressure during rigid body vibration on both position and frequency.

Extending these results to three dimensions, the values in Figs. 3 and 4 represent planes perpendicular to the vibration direction. Particularly, the minimum-pressure magnitude corresponds to a plane of minimum pressure within the entire inner ear fluid volume, approximately aligned with the centroid of the RW. It is important to note that, since the planes' orientation depends on the direction of motion, the sound pressure resulting from the rigid body vibration changes at any location depending on the vibration direction.

Figure 5 schematically illustrates such pressure distributions, in terms of the imaginary part of the sound pressure distribution with pressure values corresponding to Fig. 3, for two perpendicular directions of rigid body vibration. These illustrations show that the plane of minimum pressure

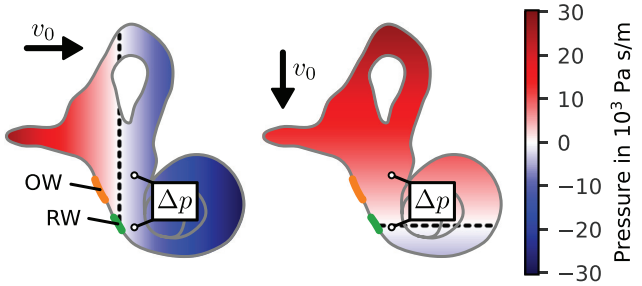

FIG. 5. Schematic illustration of two-dimensional sound pressure distributions and the determination of a differential pressure Δp, for two directions of rigid body vibration. Dashed line indicates the plane of minimum pressure. The pressure values correspond to those shown in Fig. 3.

(dashed black line) is aligned with the direction of motion and crossing the RW. This plane divides the fluid into two regions with phase difference of π (red versus blue shades). The pressure magnitude increases toward points furthest away from the RW in the direction of the vibration.

Additionally, Fig. 5 schematically depicts the determination of a differential pressure Δp between two points. The two stimulation directions show that such pressure difference strongly depends on the relative positions of the points with respect to the vibration direction. For instance, when the points are aligned within a plane perpendicular to the motion direction (left panel of Fig. 5), the differential pressure is zero. Conversely, when one point lies near the minimum-pressure plane (right panel of Fig. 5), the differential pressure magnitude is substantial.

IV. DISCUSSION

A. Underlying mechanism

The pressure distributions presented in Figs. 3–5 are governed by fundamental fluid dynamics principles. Rigid body vibration of the fluid creates regions where internal forces act predominantly as pushing (positive sound pressure) or pulling (negative sound pressure). A key insight is that the resulting pressure distribution depends solely on the position relative to the fluid volume's length in the vibration direction. This independence arises from the one-dimensional nature of the vibration. The lack of pressure gradients in directions other than the motion axis [as evidenced by Eq. (10)] ensures that the pressure remains constant within planes perpendicular to the vibration direction. Thus, the complexity and varying cross section of the inner ear geometry (e.g., the spiral-shaped scalae or the semicircular canals) are inherently accounted for by the low-frequency approximation of the fluid dynamics.

A striking result is the emergence of a plane where the pressure magnitude is minimum, located at the admittance-weighted geometric average of the fluid volume and all outlet surfaces [Eq. (14)]. If all inner ear boundaries were rigid, the minimum-pressure plane would coincide with the centroid of the fluid volume, dividing it into two equal masses. In this case, the pressure would even reach zero in magnitude, corresponding to a perfect cancellation of the pushing

and pulling effects in this plane. However, given the high compliance of the RW membrane, the minimum-pressure plane approximately shifts toward the centroid of the RW. At positions outside this plane, either the pushing or pulling effect dominates, resulting in pressure phase differences of $+\pi/2$ or $-\pi/2$ relative to the vibration velocity, as illustrated in Fig. 3. The surface admittances of the inner ear boundaries contain resistive components which introduce a small but nonzero real part in the pressure distribution [Eqs. (15) and (17)]. As a result, the pressure magnitude does not drop to zero at the minimum-pressure plane but instead reaches a small minimum value (Fig. 4). Furthermore, Eq. (14) shows that the position of the minimum plane may shift slightly with frequency due to the frequency-dependent nature of the surface admittances (Fig. 4).

The product of angular frequency, fluid density, and velocity in Eqs. (11) and (17) underscore that the observed effects are intrinsically linked to fluid inertia, in accordance with Newton's law [Eq. (10)]. Notably, these effects depend on the dimensions of the inner ear in the vibration direction (Fig. 2). Consequently, both the maximum pressure magnitudes and the orientation of the planes in the pressure distribution vary with the vibration direction, conceptually shifting $x_{\min}$ and $x_{\max}$ left or right in Fig. 4, while keeping x_0 as fixed reference point.

It is essential to distinguish the observed pressure characteristics, resulting from forced vibration of the fluid (see Chap. 7 in Rayleigh, 1945), from resonance phenomena. Resonances occur when geometric dimensions become comparable to or exceed the wavelength in the fluid, producing frequency-dependent pressure peaks and notches that may superficially resemble Fig. 4. For instance, Peterson and Bogert (1950) pointed toward a quarter wavelength resonance in the uncoiled human cochlea at approximately 12 kHz, above the frequency range of our investigation.

B. Comparison with previous works

These findings provide a theoretical explanation for the pressure distributions observed in our previous study (Kersten *et al.*, 2025, see their Fig. 6 and animations in the corresponding research data repository at https://doi.org/10.5281/zenodo.14850065), where we applied rigid body stimulation perpendicular to the OW in an anatomical finite element model of the inner ear. The numerical simulations presented in that study confirm the analytical results derived here. Notably, they demonstrated that the planar pressure distribution appears in both scala vestibuli and scala tympani with an approximately aligned plane of minimum pressure magnitude, as illustrated in Fig. 5. The simulation results further showed a slight frequency-dependent shift in the position of the minimum plane, as expressed through Eq. (14) and visible in Fig. 4. Yet, the approximate alignment of this plane with the RW centroid was previously overlooked. In contrast to the example calculations presented here, the finite element model incorporated a flexible cochlear partition. The simulations suggest that the flexibility of the cochlear partition does not substantially alter the key characteristics of the pressure distribution derived in this study at least up to 1.1 kHz, after which the distribution alternates between the derived distribution and more complex patterns (Kersten *et al.*, 2025).

In previous lumped element models of BC hearing, the fluid inertia of the inner ear was represented using acoustic masses and pressure sources (Stenfelt, 2015, 2016, 2020), or by incorporating scala vestibuli and scala tympani pressures as input variables (Guan *et al.*, 2020). These approaches inherently assume continuity of volume velocity, defined as the integral of the normal fluid particle velocity over a cross-sectional area. In contrast, our analytical approach reveals that rigid body vibration corresponds to a constant particle velocity rather than a constant volume velocity. This distinction is critical for understanding the independence of the sound pressure distribution from the cross-sectional geometry.

The explanation for this phenomenon lies in how cross-sectional changes interact with volume velocity. During rigid body vibration, unlike scenarios where the inner ear's surroundings are stationary, all surface elements contribute a volume velocity [Eq. (12)]. Thus, any change in cross section is counterbalanced by surface elements either contributing to or absorbing volume velocity. Thereby, a nearly constant particle velocity, which approximately equals the rigid body vibration velocity [Eqs. (1) and (2)], is maintained at all positions. Consequently, the pressure distribution remains unaffected by cross-sectional geometry, aligning well with the theory for low-frequency approximation of sound transmission (see Chap. 7 in Pierce, 2019).

C. Cochlear activation and comparison with AC

AC-like stimulation of the inner ear via the OW generates a relatively homogeneous sound pressure distribution within the vestibule and the basal scala vestibuli, accompanied by a gradual pressure decline along the scala tympani toward the RW, owing to the compliance of the RW membrane. This process begins with stapes motion, which introduces a differential volume velocity into the inner ear fluid volume. The BM traveling wave is then driven by a resulting pressure gradient across the base of the cochlear partition. In the literature, this pressure distribution is commonly decomposed into two components: a fast wave mode (also referred to as "compression" or "symmetric" mode), characterized by equal pressure changes in both scalae due to overall fluid compression from stapes motion; and a slow wave mode (or "antisymmetric" mode), which represents the pressure difference between scala vestibuli and scala tympani related to the BM traveling wave (Peterson and Bogert, 1950; Olson, 1998; Kim *et al.*, 2011; Olson, 2013).

For rigid body vibration, the fast wave mode arises from fluid acceleration rather than compression. This inertial mechanism inherently produces a pressure gradient throughout the cochlear fluid [Eq. (9)], even in the absence of differential volume velocities at the boundaries. In this case, the

https://doi.org/10.1121/10.0039575

pressure gradient is a primary effect of the stimulation and exists independently of the BM traveling wave. This contrasts sharply with OW stimulation, highlighting both a fundamental difference in the nature of the fast wave component and a fundamental difference in the origin of the differential pressure that drives the BM traveling wave.

Importantly, this does not imply the absence of a BM traveling wave during vibrational stimulation. Rather, as long as the assumption of small local differential velocities (e.g., those associated with cochlear partition motion) holds, these differential motions may still produce localized pressure differences that are superimposed on the inertial pressure field described above, analogous to the superposition of fast and slow waves in OW stimulation. Thus, our analysis aligns with the prevailing understanding that the traveling wave formation does not fundamentally differ between AC and BC hearing (von Békésy, 1960).

D. Differential intracochlear sound pressures

Given its direct relation to traveling wave excitation, the differential intracochlear sound pressure between OW and RW can be interpreted as an indicator for auditory stimulation. This has motivated the experimental approach employing two pressure probes inserted into the scala vestibuli and scala tympani at the cochlear base. Under AC stimulation, the relatively uniform intracochlear pressure distribution allows such two-point measurements to reliably capture the differential pressure that drives the BM traveling wave (Nakajima *et al.*, 2009; Stieger *et al.*, 2018). In contrast, during rigid body vibration, pressure differences align with the direction of motion (Fig. 5), rather than primarily between the OW and RW, as in AC stimulation. Such measured pressure differences during vibrational stimulation depend not only on the vibration's orientation, magnitude, and phase, but, most critically, on the precise locations of the measurement probes (Fig. 4). This spatial dependence underscores that the exact positioning of pressure sensors is much more critical under BC stimulation than under AC stimulation, highlighting current limitations in capturing the specific sound pressure driving the BM traveling wave using measurements at only two intracochlear locations.

Furthermore, the fundamental principles considered here also help explain the high variability widely reported for experimental differential pressure measurements under BC stimulation (Stieger *et al.*, 2018; Borgers *et al.*, 2019; Dobrev *et al.*, 2023; Geerardyn *et al.*, 2024). To assess the role of the involved phenomena more precisely, two factors require consideration: (1) the direction of inner ear vibration, and (2) the interaction between fluid inertia and other BC mechanisms.

1. Directions of inner ear vibration

During intracochlear pressure measurements in temporal bones, the vibration directions vary across specimens and fluctuate with frequency (Stieger *et al.*, 2018). For cadaver head measurements and finite element simulations using a full-head model, Dobrev *et al.* (2023) and Dobrev *et al.* (2025) reported that the common motion component in the vibration of the otic capsule, corresponding to rigid body vibration, was at least 10 dB higher than the differential motion component up to approximately 7–10 kHz. Instead of a specific direction of motion, the magnitude and phase relationship between the orthogonal vibration components are complex (Dobrev and Sim, 2018), influenced by translational and rotational skull vibration at low frequencies, and skull deformation at higher frequencies (Lim *et al.*, 2023).

As previously mentioned, the resulting pressure distribution from such velocity components, each with varying magnitudes and phases, can be understood as the superposition of the individual distributions corresponding to each component. Depending on the magnitude and phase relationship between these components, this can lead to different orientations of the sound pressure planes or even a line of minimum pressure magnitude instead of a plane. Furthermore, as the velocity vector components fluctuate with frequency (Dobrev and Sim, 2018), these characteristics shift unpredictably. This variability likely contributes to fluctuations observed in differential pressure measurements during BC stimulation.

2. Interaction of BC mechanisms

This study focuses on the sound pressure distribution resulting from fluid dynamics under rigid body vibration. However, additional contributors to the sound pressure include deformation of the inner ear (Tonndorf, 1962; Stenfelt, 2015), sound transmission through the vestibular and cochlear aqueducts (Freeman *et al.*, 2000; Sohmer and Freeman, 2004; Dobrev *et al.*, 2022), and sound entering via the OW from the ear canal and middle ear (Tonndorf, 1968; Stenfelt and Goode, 2005a). As pointed out in prior research (Taschke, 2005; Stenfelt, 2016, 2020; Kersten *et al.*, 2025), these BC mechanisms can be described using the principle of superposition. Our considerations highlight that this principle must be applied in a location-dependent manner, summing the distinct sound pressure distributions associated with each mechanism.

Unlike the rigid body vibration component, the additional mechanisms arise from deformation of the cochlear boundaries, leading to pressure distributions that differ from the planar patterns we derived for fluid inertia. For instance, deformation of the vestibule can be expected to generate pressure distributions similar to those with AC stimulation, with a homogeneous sound pressure distribution in the vestibule and basal part of scala vestibuli, and a pressure decrease toward the RW membrane. These mechanisms likely fill the minimum-pressure plane associated with the fluid-inertia distribution and aligned with the RW centroid.

E. Role of the RW

Notably, the RW plays a role in the pressure distributions for the different types of inner ear stimulation involved in BC through different mechanisms. For OW input, RW

compliance is essential for establishing the pressure gradient across the cochlear partition, as shown by reduced differential pressures after RW reinforcement (Liyanage *et al.*, 2021; Guan *et al.*, 2018; Geerardyn *et al.*, 2024). In contrast, Geerardyn *et al.* (2024) observed that RW reinforcement during BC stimulation produced little change in the average intracochlear pressure, although individual responses varied substantially. The factors outlined above help explain these findings, even assuming negligible contributions from BC mechanisms other than rigid body vibration.

Our derivation predicts that RW stiffening can shift the position of the minimum-pressure plane, causing pronounced changes in intracochlear pressures in individual cases. However, because the direction of inner-ear vibration varies with both frequency and specimen (Dobrev and Sim, 2018), such shifts are unlikely to produce consistent changes in pressure magnitudes across frequencies or across ears, consistent with the averaged results of Geerardyn *et al.* (2024). Moreover, scala tympani pressures are typically recorded apical to the RW rather than at its centroid (see, e.g., Stieger *et al.*, 2018, their Fig. 1), making it unlikely that measurement sites coincide with the pressure minimum for most vibration directions and frequencies.

F. Limitations and suggestions for future work

1. Rotational rigid body vibration

To analytically elucidate the spatial dependence of intracochlear sound pressure under rigid body vibration, we adopted the simplifying assumption of a nearly uniform vibration velocity across the entire fluid volume [Eq. (2)]. Strictly speaking, this assumption does not hold for rotational rigid body vibration of the inner ear. However, such motion arises primarily from head rotation during BC stimulation, which has been reported to occur around the skull's center of mass (Lim *et al.*, 2023). Since this center lies outside the inner ear volume, we hypothesize that rotational motion yields pressure characteristics similar to those derived for translational motion, with the key distinction that the planes of equal pressure are perpendicular to the tangential velocity of the rotation, rather than being parallel to each other. Future studies should investigate this hypothesis to confirm the pressure distributions associated with rotational rigid body vibration of the inner ear.

2. Interaction of BC mechanisms

While AC pressure distributions have been extensively studied [e.g., Peterson and Bogert (1950); Siebert (1974); Taber and Steele (1981); Olson (2013)], further theoretical work is required to extend these insights to BC mechanisms, where the entire cochlear boundary vibrates. In particular, consistent with our omission of differential velocities [Eqs. (1) and (2)], our analysis does not account for local effects, such as those associated with the BM traveling wave. Moreover, we excluded any BC component that is not related to the rigid body vibration of the inner ear by treating the two windows and other outlets as passive surfaces. Finite element simulations (Taschke, 2005; Kim *et al.*, 2014; Lim *et al.*, 2022; Kersten *et al.*, 2024) could bridge this gap and provide a more comprehensive understanding of the pressure distributions associated with different BC mechanisms and their interactions.

3. Experimental validation

Our findings offer a theoretical explanation for the characteristics and underlying mechanisms of measured intracochlear sound pressures. However, experimental data directly confirming the predicted pressure distributions resulting from rigid body vibration are not yet available. This limitation is due to the various factors involved in BC stimulation of the inner ear outlined above. Nevertheless, the theoretical insights gained from this study can serve as a foundation for the design of future experiments aimed at validating these predictions. Such validation would require:

- Separating the effects of rigid body vibration from other BC mechanisms — particularly those involving stimulation via the OW — for example, by glueing the stapes to the adjacent bone (Stenfelt *et al.*, 2002).
- Stimulating inner ear specimen with vibration in a single, controlled direction, which can be approximately achieved in temporal bone preparations (Stenfelt *et al.*, 2003).
- Measuring the intracochlear sound pressure distribution along the direction of vibration, for instance, by precisely positioning a pressure sensor using a mechanical guide that moves in unison with the vibrating specimen.

4. Interpretation of experimental data

Finally, while the analytical approach used in this study does not directly yield practical conclusions about the perception of BC sound, it addresses critical aspects concerning the interpretation of objective measurements in relation to auditory perception.

First, the findings suggest that further theoretical and numerical investigations are required to identify optimal probe placement for capturing the pressures most representative of BM stimulation, with spatial accuracy beyond what has been necessary for AC stimulation. Follow-up experimental studies will be essential to assess the practical feasibility of implementing such targeted measurements. Until then, interpreting the characteristics of differential pressure measurements from BC stimulation as equivalent to those from AC stimulation should be approached with caution.

Second, cochlear vibration levels are commonly used to evaluate BC stimulation effectiveness, for instance, when comparing BC transducers or stimulation locations (Stenfelt and Goode, 2005b; Eeg-Olofsson *et al.*, 2008; Håkansson *et al.*, 2010; Dobrev *et al.*, 2016; Rigato *et al.*, 2019; Chang and Stenfelt, 2019; Ghoncheh *et al.*, 2022; Prodanovic and Stenfelt, 2021; Wils *et al.*, 2024; du Puits *et al.*, 2025). Our analysis supports the general assumption that higher vibration velocities lead to higher intracochlear pressures,

consistent with fluid inertia-driven responses. However, at a given velocity, intracochlear pressure can vary significantly with spatial location (Figs. 4 and 5). As a result, directly linking vibration levels to auditory perception is nontrivial, given the unresolved questions surrounding the differential pressure driving BM motion and the interactions with other BC mechanisms. These insights echo previous findings showing low correlation between promontory vibration and perceptual outcomes (Eeg-Olofsson *et al.*, 2013), as well as observed discrepancies between promontory and BM velocities (Lim *et al.*, 2023).

V. CONCLUSION

We presented an analytical approach to capture intracochlear sound pressure distributions induced by rigid body vibration of the inner ear. Our analysis demonstrates that the vibration at a spatially uniform velocity along a single direction leads to:

- pressure proportionality to stimulation velocity and frequency;
- a linear pressure gradient along the vibration direction;
- uniform pressure in planes perpendicular to the motion; and
- a plane with minimum pressure magnitude approximately aligned with the centroid of the RW membrane.

For an arbitrary complex-valued velocity vector of the rigid body translation, the pressure distribution can be determined by superimposing the individual distributions corresponding to each velocity component.

These findings provide explanations for the significant variability observed in measurements while highlighting the need for further investigations of the interactions between fluid inertia and other BC mechanisms to refine theoretical models and improve the interpretation of experimental data.

SUPPLEMENTARY MATERIAL

See the supplementary material for the Python code used to calculate the sound pressure distributions presented in Figs. 3 and 4.

ACKNOWLEDGMENTS

This work was funded by the Deutsche Forschungsgemeinschaft (DFG, German Research Foundation) – Project-ID 352015383 – SFB 1330 A4.

AUTHOR DECLARATIONS

Conflict of Interest

All authors declare that they have no conflicts of interest.

DATA AVAILABILITY

The data that support the findings of this study are available within the article and its supplementary material.

Borgers, C., Fierens, G., Putzeys, T., van Wieringen, A., and Verhaert, N. (**2019**). "Reducing artifacts in intracochlear pressure measurements to study sound transmission by bone conduction stimulation in humans," Otol. Neurotol. **40**(9), e858–e867.
Chang, Y., and Stenfelt, S. (**2019**). "Characteristics of bone-conduction devices simulated in a finite-element model of a whole human head," Trends Hear. **23**, 233121651983605.
Dancer, A., and Franke, R. (**1980**). "Intracochlear sound pressure measurements in guinea pigs," Hear. Res. **2**(3), 191–205.
Dobrev, I., Farahmandi, T., Pfiffner, F., and Röösli, C. (**2022**). "Intracochlear pressure in cadaver heads under bone conduction and intracranial fluid stimulation," Hear. Res. **421**, 108506.
Dobrev, I., Lim, J., Kim, N., Niermann, J., Röösli, C., and Pfiffner, F. (**2025**). "Exploration of the dynamics of otic capsule and intracochlear pressure: Numerical insights with experimental validation," J. Acoust. Soc. Am. **157**(1), 554–568.
Dobrev, I., Pfiffner, F., and Röösli, C. (**2023**). "Intracochlear pressure and temporal bone motion interaction under bone conduction stimulation," Hear. Res. **435**, 108818.
Dobrev, I., and Sim, J. H. (**2018**). "Magnitude and phase of three-dimensional (3D) velocity vector: Application to measurement of cochlear promontory motion during bone conduction sound transmission," Hear. Res. **364**, 96–103.
Dobrev, I., Stenfelt, S., Röösli, C., Bolt, L., Pfiffner, F., Gerig, R., Huber, A., and Sim, J. H. (**2016**). "Influence of stimulation position on the sensitivity for bone conduction hearing aids without skin penetration," Int. J. Audiol. **55**(8), 439–446.
du Puits, A., Åsnes, K., Lenarz, T., and Maier, H. (**2025**). "Investigation of bone conduction stimulation efficiency on the skull surface and below assessed by cochlear promontory vibration," Hear. Res. **462**, 109280.
Eeg-Olofsson, M., Stenfelt, S., Taghavi, H., Reinfeldt, S., Håkansson, B., Tengstrand, T., and Finizia, C. (**2013**). "Transmission of bone conducted sound: Correlation between hearing perception and cochlear vibration," Hear. Res. **306**, 11–20.
Eeg-Olofsson, M., Stenfelt, S., Tjellström, A., and Granström, G. (**2008**). "Transmission of bone-conducted sound in the human skull measured by cochlear vibrations," Int. J. Audiol. **47**(12), 761–769.
Frear, D. L., Guan, X., Stieger, C., Rosowski, J. J., and Nakajima, H. H. (**2018**). "Impedances of the inner and middle ear estimated from intracochlear sound pressures in normal human temporal bones," Hear. Res. **367**, 17–31.
Freeman, S., Sichel, J.-Y., and Sohmer, H. (**2000**). "Bone conduction experiments in animals: Evidence for a non-osseous mechanism," Hear. Res. **146**(1), 72–80.
Geerardyn, A., Wils, I., Putzeys, T., Fierens, G., Wouters, J., and Verhaert, N. (**2024**). "The impact of round window reinforcement on middle and inner ear mechanics with air and bone conduction stimulation," Hear. Res. **450**, 109049.
Ghoncheh, M., Stenfelt, S., Maas, P., Salcher, R., Prenzler, N., Raufer, S., and Maier, H. (**2022**). "Output performance of the novel active transcutaneous bone conduction implant Sentio at different stimulation sites," Hear. Res. **421**, 108369.
Guan, X., Cheng, Y., Galaiya, D., Rosowski, J., Lee, D., and Nakajima, H. (**2020**). "Bone-conduction hyperacusis induced by superior canal dehiscence in human: The underlying mechanism," Sci. Rep. **10**(1), 16564.
Guan, X., Cheng, Y. S., Galaiya, D., and Nakajima, H. H. (**2018**). "The effect of round window reinforcement on human hearing," AIP Conf. Proc. **1965**(1), 150004.
Håkansson, B., Reinfeldt, S., Eeg-Olofsson, M., Östli, P., Taghavi, H., Adler, J., Gabrielsson, J., Stenfelt, S., and Granström, G. (**2010**). "A novel bone conduction implant (BCI): Engineering aspects and pre-clinical studies," Int. J. Audiol. **49**(3), 203–215.
Hiller, J., Nour-Eldin, N.-E. A., Gruber-Rouh, T., Burck, I., Harth, M., Stöver, T., Vogl, T., and Naguib, N. N. N. (**2020**). "Assessing inner ear volumetric measurements by using three-dimensional reconstruction imaging of high-resolution cone-beam computed tomography," SN Compr. Clin. Med. **2**(11), 2178–2184.
Kersten, S., Taschke, H., and Vorländer, M. (**2024**). "Influence of the cochlear partition's flexibility on the macro mechanisms in the inner ear," Hear. Res. **453**, 109127.
Kersten, S., Taschke, H., and Vorländer, M. (**2025**). "Finite element analysis of the osseous spiral lamina's influence on inner ear fluid flow during bone conduction stimulation," Hear. Res. **459**, 109205.

Kim, N., Homma, K., and Puria, S. (**2011**). "Inertial bone conduction: Symmetric and anti-symmetric components," J. Assoc. Res. Otolaryngol. **12**(3), 261–279.
Kim, N., Steele, C. R., and Puria, S. (**2014**). "The importance of the hook region of the cochlea for bone-conduction hearing," Biophys. J. **107**(1), 233–241.
Lim, J., Dobrev, I., and Kim, N. (**2023**). "Reference velocity of a human head in bone conduction hearing: Finite element study," Hear. Res **429**, 108699.
Lim, J., Dobrev, I., Röösli, C., Stenfelt, S., and Kim, N. (**2022**). "Development of a finite element model of a human head including auditory periphery for understanding of bone-conducted hearing," Hear. Res. **421**, 108337.
Liyanage, N., Prochazka, L., Grosse, J., Dalbert, A., Tabibi, S., Chatzimichalis, M., Dobrev, I., Kleinjung, T., Huber, A., and Pfiffner, F. (**2021**). "Round window reinforcement-induced changes in intracochlear sound pressure," Appl. Sci. **11**, 5062.
Marburg, S., and Anderssohn, R. (**2011**). "Fluid structure interaction and admittance boundary conditions: Setup of an analytical example," J. Comput. Acoust. **19**(1), 63–74.
Mattingly, J. K., Banakis Hartl, R. M., Jenkins, H. A., Tollin, D. J., Cass, S. P., and Greene, N. T. (**2020**). "A comparison of intracochlear pressures during ipsilateral and contralateral stimulation with a bone conduction implant," Ear Hear. **41**(2), 312–322.
Nakajima, H. H., Dong, W., Olson, E. S., Merchant, S. N., Ravicz, M. E., and Rosowski, J. J. (**2009**). "Differential intracochlear sound pressure measurements in normal human temporal bones," J. Assoc. Res. Otolaryngol. **10**(1), 23–36.
Olson, E. S. (**1998**). "Observing middle and inner ear mechanics with novel intracochlear pressure sensors," J. Acoust. Soc. Am. **103**(6), 3445–3463.
Olson, E. S. (**2013**). "Fast waves, slow waves and cochlear excitation," Proc. Mtgs. Acoust. **19**(1), 050134.
Peterson, L. C., and Bogert, B. P. (**1950**). "A dynamical theory of the cochlea," J. Acoust. Soc. Am. **22**(3), 369–381.
Pierce, A. (**2019**). *Acoustics: An Introduction to Its Physical Principles and Applications*, 3rd ed. (Springer, New York).
Prodanovic, S., and Stenfelt, S. (**2021**). "Review of whole head experimental cochlear promontory vibration with bone conduction stimulation and investigation of experimental setup effects," Trends Hear. **25**, 23312165211052764.
Purcell, D., Johnson, J., Fischbein, N., and Lalwani, A. K. (**2003**). "Establishment of normative cochlear and vestibular measurements to aid in the diagnosis of inner ear malformations," Otolaryngol. Head Neck Surg. **128**(1), 78–87.
Puria, S. (**2003**). "Measurements of human middle ear forward and reverse acoustics: Implications for otoacoustic emissions," J. Acoust. Soc. Am. **113**(5), 2773–2789.
Rayleigh, J. W. S. (**1945**). *The Theory of Sound*, 2nd ed. (Dover, Mineola, NY), Vol. 2.
Rigato, C., Reinfeldt, S., Håkansson, B., Fredén Jansson, K.-J., Renvall, E., and Eeg-Olofsson, M. (**2019**). "Effect of transducer attachment on vibration transmission and transcranial attenuation for direct drive bone conduction stimulation," Hear. Res. **381**, 107763.
Siebert, W. M. (**1974**). "Ranke revisited: A simple short-wave cochlear model," J. Acoust. Soc. Am. **56**(2), 594–600.
Sohmer, H., and Freeman, S. (**2004**). "Further evidence for a fluid pathway during bone conduction auditory stimulation," Hear. Res. **193**(1), 105–110.
Stenfelt, S. (**2015**). "Inner ear contribution to bone conduction hearing in the human," Hear. Res. **329**, 41–51.
Stenfelt, S. (**2016**). "Model predictions for bone conduction perception in the human," Hear. Res. **340**, 135–143.
Stenfelt, S. (**2020**). "Investigation of mechanisms in bone conduction hyperacusis with third window pathologies based on model predictions," Front. Neurol. **11**, 966.
Stenfelt, S., and Goode, R. L. (**2005a**). "Bone-conducted sound: Physiological and clinical aspects," Otol. Neurotol. **26**(6), 1245–1261.
Stenfelt, S., and Goode, R. L. (**2005b**). "Transmission properties of bone conducted sound: Measurements in cadaver heads," J. Acoust. Soc. Am. **118**(4), 2373–2391.
Stenfelt, S., Hato, N., and Goode, R. L. (**2002**). "Factors contributing to bone conduction: The middle ear," J. Acoust. Soc. Am. **111**(2), 947–959.
Stenfelt, S., Puria, S., Hato, N., and Goode, R. L. (**2003**). "Basilar membrane and osseous spiral lamina motion in human cadavers with air and bone conduction stimuli," Hear. Res. **181**(1), 131–143.
Stieger, C., Guan, X., Farahmand, R. B., Page, B. F., Merchant, J. P., Abur, D., and Nakajima, H. H. (**2018**). "Intracochlear sound pressure measurements in normal human temporal bones during bone conduction stimulation," J. Assoc. Res. Otolaryngol. **19**(5), 523–539.
Suzuki, S., Maruyama, S., and Ido, H. (**1989**). "Boundary element analysis of cavity noise problems with complicated boundary conditions," J. Sound Vib. **130**(1), 79–96.
Taber, L. A., and Steele, C. R. (**1981**). "Cochlear model including three-dimensional fluid and four modes of partition flexibility," J. Acoust. Soc. Am. **70**(2), 426–436.
Taschke, H. (**2005**). "Mechanismen der Knochenschallleitung" ("Mechanisms of bone-conducted sound"), Ph.D. thesis, Ruhr University Bochum, Bochum, Germany.
Tonndorf, J. (**1962**). "Compressional bone conduction in cochlear models," J. Acoust. Soc. Am. **34**(8), 1127–1131.
Tonndorf, J. (**1968**). "A new concept of bone conduction," Arch. Otolaryngol. **87**(6), 595–600.
von Békésy, G. (**1960**). *Experiments in Hearing* (McGraw-Hill, New York).
Wils, I., Geerardyn, A., Putzeys, T., Fierens, G., Denis, K., and Verhaert, N. (**2024**). "Objective preclinical measures for bone conduction implants," Front. Neurosci. **18**, 1324971.